

Laser-controlled tandem catalytic sites of CuNi alloy with ampere-level electrocatalytic nitrate to ammonia activity for Zn–nitrate battery

Wanqiang Yu^{a#}, Jiayuan Yu^{a#}, Man Huang^a, Yujie Wang^a, Yijie Wang^a, Jiawei Li^a,
Hong Liu^{a,b}, Weijia Zhou^{a*}

^aInstitute for Advanced Interdisciplinary Research (iAIR), School of Chemistry and Chemical Engineering, University of Jinan, Jinan, 250022, P. R. China.

^bState Key Laboratory of Crystal Materials, Shandong University, Jinan, 250100, P. R. China.

*Corresponding authors. E-mail: ifc_zhouwj@ujn.edu.cn (W. Zhou).

These authors contributed equally to this work

Experimental Section

Chemicals

Hydrochloric acid (HCl), phosphoric acid (H₃PO₄), sulfamic acid (H₃NO₃S), salicylic acid (C₇H₆O₃), sodium hypochlorite (NaClO), sodium hydroxide (NaOH), Sodium nitrite (NaNO₃), sodium nitrite (NaNO₂), ammonium chloride (NH₄Cl) and sodium sulfate (Na₂SO₄) were purchased from Sinopharm Chemical Reagent Co., Ltd. Sodium nitroferricyanide dihydrate (C₅FeN₆Na₂O·2H₂O), potassium sodium tartrate tetrahydrate (C₄H₄O₆KNa·4H₂O), sulfanilamide (C₆H₈N₂O₂S), N-(1-naphthyl) ethylenediamine dihydrochloride (C₁₂H₁₄N₂·2HCl) were purchased from Shanghai Macklin Biochemical Co., Ltd. Sodium nitrate-¹⁵N (Na¹⁵NO₃) and ammonium chloride-¹⁵N (¹⁵NH₄Cl) were purchased from Shanghai Aladdin Biochemical Technology Co.,Ltd. Deionized water (18.2 MΩ cm) was produced by the Thermo Scientific Barnstead Smar2Pure Ultrapure Water System. Copper foils (99.99%) and nickel foils (99.99%) were purchased from Dahe New Energy Co., Ltd. Unless otherwise stated, all reagents were used without further purification.

Synthesis of copper-nickel alloy nanoparticles loaded on the copper foil (CuNi NPs/CF)

Pulsed ultraviolet (UV) laser (Pulse 355-3, Shanghai Fermi Laser Technology Co., Ltd.) was used to synthesize CuNi. First, Ni foil and Cu foil were cleaned with anhydrous ethanol and DI water for 10 minutes to remove organic matters and impurities on the surface. Second, Ni foil with 0.02 mm thickness on Cu foil with 0.1 mm thickness was put on the vibration reduction table of the nanosecond pulsed UV laser device with the wavelength of 355 nm to ensure the accuracy, which was also equipped with vacuum pump to keep the metal sheets close-contact. Then, Cu foil was processed by laser scanning with the certain power (0.9 W), which was set by the software installed on computer. In the process of scanning, the laser-treated Ni foil fused and combined with Cu foil below. The black Cu-Ni catalyst supported on Cu foil were obtained and cleaned by ultrasonic for 5 seconds to remove the residual powder, following dried by N₂ flow. The samples of Cu nanoparticles loaded on Cu foil (Cu NPs/CF) and Ni nanoparticles loaded on Ni foil (Ni NPs/NF) as comparison samples were also prepared. The synthesis process of the Cu NPs/CF and Ni NPs/NF was similar with that of CuNi NPs/CF.

Characterization

The crystal structure of the prepared electrocatalysts were determined by Smartlabse (RIGAKU) X-ray diffractometer (XRD) with Cu K α radiation ($\lambda=0.15406$ nm). The microstructure and morphology were clarified by Regulus 8100 (HITACHI) Field Emission Scanning Electron Microscope (FESEM) and JEM-2100F (JEOL) transmission electron microscope (TEM) at an acceleration voltage of 200 kV. The elemental composition and chemical environment of the materials were characterized by Axis Supra (Kratos) X-ray photoelectron spectroscopic (XPS). Raman spectra were collected using a LabRAM HR Evolution spectrometer (Horiba). A UV-vis spectrophotometer (EVOLUTION 201, Thermo Scientific Corporation) measurements in the range of 200-1000 nm. $^1\text{H-NMR}$ measurements were performed on Bruker AVANCE III HD 600 MHz Nuclear Magnetic Resonance System (NMR-600). X-ray absorption fine structure (XAFS) measurements of the Cu K-edge and Ni K-edge in transmission mode for Cu foil, Ni foil and sample of CuNi NPs were performed at Beijing Synchrotron Radiation Facility (BL1W1B station), China.

Electrochemical measurements

Electrochemical measurements of nitrate reduction reaction (NIRR)

The electrochemical measurements were carried out using a CHI 760E electrochemical workstation (Chenhua, Shanghai) in a H-type electrolytic cell separated by a Nafion211 membrane. The CuNi NPs/CF, Hg/HgO and platinum foil was used as the working electrode, reference electrode and counter electrode, respectively. And the working electrode with the area of $0.5 \times 0.5 \text{ cm}^2$ was treated on both sides by laser. 70 mL 1 M NaOH solution was distributed to the anode compartment. And 70 mL 1 M NaOH and $44.3 \text{ g L}^{-1} \text{ NO}_3^-$ solution was added into the cathode compartment for NO_3^- reduction. Before NO_3^- electroreduction test, LSV curves were performed until that the polarization curves achieve steady-state ones at a rate of 10 mV s^{-1} from 0.6 to -0.68 V vs. RHE . The potentiostatic tests were conducted at a series of applied potentials in a typical H-type cell on the electrochemical workstation with a stirring rate of 300 rpm in 2 hours. Cyclic voltammetry (CV) curves in C_{dl} determination were measured in a potential window nearly without the Faradaic process at different scan rates of 20, 40, 60, 80 and 100 mV s^{-1} . The plot of current density at set potential against scan rate had a linear relationship and its slope was the C_{dl} . EIS measurement was carried out in an H-type

cell at a series of applied potentials in the frequency range from 0.1 Hz to 10^5 Hz with 5 mV amplitude in 1 M NaOH with and without $44.3 \text{ g L}^{-1} \text{ NO}_3^-$.

The ultraviolet-visible (UV-Vis) spectrophotometer was used to detect the ions (NO_3^- and NH_4^+) concentration of pre-test and post-test electrolytes after diluting to appropriate concentration to match the range of calibration curves. The specific detection methods were presented in the **Text S1**. The concentrations of feed and electrolytic products were analyzed by UV spectrophotometry. (**Fig. S11**).

Text S1. Determination of ion concentration

The ultraviolet-visible (UV-Vis) spectrophotometer was used to detect the ion concentration of pre- and post-test electrolytes after diluting to appropriate concentration to match the range of calibration curves. The specific detection methods are as follow.

Determination of nitrate-N

Firstly, a certain amount of electrolyte was taken out from the electrolytic cell and diluted to 5 mL to detection range. Then, 0.1 mL 1 M HCl and 0.01 mL 0.8 wt% sulfamic acid solution were added into the aforementioned solution. The absorption spectrum was measured using an UV-Vis spectrophotometer and the absorption intensities at a wavelength of 220 was recorded. The concentration-absorbance curve was calibrated using a series of standard potassium nitrate solutions and the potassium nitrate crystal was dried at 105-110 °C for 2 h in advance.

Determination of ammonia-N

Ammonia-N was determined using salicylic acid-potassium sodium tartrate chromogenic reagent as the color reagent. First, a certain amount of electrolyte was taken out from the electrolytic cell and diluted to 5 mL to detection range. Next, 0.5 mL salicylic acid-potassium sodium tartrate chromogenic reagent was added and mixed thoroughly, then 0.05 mL sodium nitroprusside and 0.05 mL sodium hypochlorite solution were put into the solution. The absorption intensity at a wavelength of 675 nm was recorded after sitting for 1 h. The concentration-absorbance curve was calibrated using a series of standard ammonium chloride solutions and the ammonium chloride crystal was dried at 105 °C for 2 h in advance.

Isotope Labeling Experiments.

99.21% $\text{Na}^{15}\text{NO}_3$ was used as the feeding N-source to perform the isotopic labeling

nitrate reduction experiments to clarify the source of ammonia. 1 M NaOH was used as electrolyte and Na¹⁵NO₃ with a concentration of 44.3 g L⁻¹ ¹⁵NO₃⁻ was added into the cathode compartment as the reactant. After electroreduction, electrolyte with obtained ¹⁵NH₄⁺ was taken out and the pH value was adjusted to be weak acid with 4 M H₂SO₄ for further quantification by ¹H NMR (600 MHz) with external standards of maleic acid.

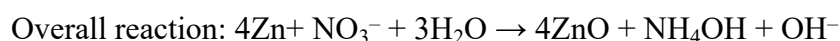
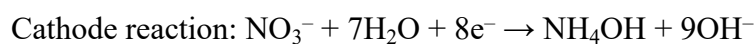
Electron paramagnetic resonance spectroscopy experiments

First, the electrocatalytic test on CuNi NPs/CF, Cu NPs/CF and Ni NPs/NF was conducted in 1 M NaOH solution with or without 44.3 g L⁻¹ NO₃⁻ at -0.48 V vs. Hg/HgO for 3 minutes. After that, 0.8 mL of electrolyte was taken out from cathode chamber in time, and 25 mg DMPO was added into the electrolyte. Then, electron paramagnetic resonance spectrum was measured.

Assembly of the Zn-NO₃⁻ battery

The CuNi NPs/CF and Zn plate were employed as the cathode and anode for Zn-NO₃⁻ battery, respectively. A typical H-type cell that contains 70 mL cathode electrolyte (3.5 M NaOH + 44.3 g L⁻¹ NO₃⁻) and 70 mL anode electrolyte (3.5 M NaOH) separated by a bipolar membrane. The discharging polarization curves with a scan rate of 5 mV/s and galvanostatic tests were conducted using CHI 760E workstation and Land 2001A battery test system at room temperature, respectively. After electrochemical test, the electrolyte was diluted to a certain concentration for the next detection. The power density (P) of Zn-NO₃⁻ battery was determined by $P = I \times V$, where I and V are the discharge current density and voltage, respectively.

The electrochemical reactions in Zn-NO₃⁻ battery were presented as following:



Calculation of electrode potential for half reaction of cathode and anode

Since cathode and anode of Zn-NO₃⁻ are separated by a bipolar membrane, the electrode potentials should be calculated individually:

$$E_{\text{anode}} = -\frac{1}{nF}(\Delta G_{\text{ano}} + RT \ln \frac{1}{[\text{OH}^-]^2})$$

$$E_{cathode} = -\frac{1}{nF} \left(\Delta G_{cat} + RT \ln \frac{[OH^-]^9 [NH_4OH]}{[NO_3^-]} \right)$$

Where n, F, ΔG, R, and T are electron transfer number, the Faraday constant (96485 C/mol), standard molar Gibbs free energy change of chemical reaction at 298 K, gas constant (8.314 J/ (mol K)), and reaction temperature (298 K), respectively.

In the electrolyte system of 3.5 M NaOH || 3.5 M NaOH + 44.3 g L⁻¹ NO₃⁻.

The concentrations of [OH⁻] in cathode cell and anode cell are 3.5 and 3.5 mol L⁻¹, respectively. [NO₃⁻] is 10 g L⁻¹. Assuming [NH₄OH] is 10⁻³ mol L⁻¹ in cathode cell.

$$E_{anode} = -\frac{1}{nF} \left(\Delta G_{ano} + RT \ln \frac{1}{[OH^-]^2} \right) = -1.26 V$$

$$E_{cathode} = -\frac{1}{nF} \left(\Delta G_{cat} + RT \ln \frac{[OH^-]^9 [NH_4OH]}{[NO_3^-]} \right) = -0.15 V$$

$$E_{anode} = E_{cathode} - E_{anode} = 1.11 V$$

Computational Method

All density functional theory calculations were performed by Vienna ab initio simulation package (VASP). (*Phys. Rev. B* 54 (1996) 11169.) The Perdew-Burke-Ernzerhof (PBE) (*Phys. Rev. Lett.* 77 (1996) 3865.) functional was employed to treat the exchange-correlation interactions. The plane-wave basis set with a kinetic energy cutoff of 400 eV, the energy convergence criterion of 10⁻⁴ eV, the force convergence criterion of 0.02 eV Å⁻¹, and a (2×2×1) Monkhorst-Pack k-point sampling was employed for structure relaxation. For different surface models, the bottom layer was fixed. A sufficiently large vacuum gap (> 12 Å) was employed to prevent the interaction between neighboring periodic structures. H₂, HNO₃ and H₂O were calculated in boxes of 20 Å×20 Å×20 Å with the gamma point only. The free energy diagrams for Nitrate reduction to Ammonia were calculated with reference to the computational hydrogen electrode. (*J. Phys. Chem. B* 108 (2004) 17886–17892.) The free energy of gas phase and adsorbed species can be obtained from the following equation:

$$G = E_{\text{elec}} + ZPE - TS$$

where E_{elec} is the electronic energy.

To avoid describing the charged NO_3^{-1} species as a reference within periodic DFT calculations, a thermodynamic cycle from NO_3^{-1} to NO_3 was adapted. Considering entropic and enthalpic contributions, we applied 0.75 eV correction to compensating the DFT calculation. (ACS Catal. 2019, 9, 7052–7064.) The Gibbs free energy of nitrate adsorption from the solution phase at 0 V vs. reverse hydrogen electrode (RHE) is presented by eq:

$$\Delta G_{\text{NO}_3=\text{E}(*\text{NO}_3)} = \frac{1}{2}E(\text{H}_2) - E(*) - E(\text{HNO}_3) + 0.75 \text{ eV}$$

Direct ammonia product synthesis.

First, the downstream electrolyte product during the long-term discharge stability test of Zn- NO_3^- battery by CuNi NPs/CF as the cathode at 225 mA cm^{-2} for 120 h in a flow-system H cell was collected. To evaluate the NH_3 removal efficiency via air stripping and the NH_3 collection efficiency by acid trap, 350 ml of downstream product was sealed in a flask with 200 sccm Ar gas flowing in for 24 h to perform the air stripping to purge the NH_3 out. The outlet gas stream was meanwhile purged into 50 ml of 3 M HCl to collect the NH_3 product. The amount of NH_3 in all the solutions was measured by the ammonia detection method mentioned above, and the removal efficiency and collection efficiency were calculated based on equations as follows:

$$\text{Removed } \text{NH}_3 \text{ via air stripping} = 1 - \frac{\text{NH}_3 \text{ left after air stripping (mol)}}{\text{initial } \text{NH}_3 \text{ (mol)}}$$

$$\text{Acid collected } \text{NH}_3 = \frac{\text{NH}_3 \text{ in acid trap (mol)}}{\text{Removed } \text{NH}_3 \text{ via air stripping (mol)}}$$

To produce the $\text{NH}_4\text{Cl(s)}$ product and evaluate the production efficiency, the 50 ml of HCl with the trapped NH_3 was dried by rotary evaporator, and the collected powder sample was further dried at 80 °C in an oven overnight. The final $\text{NH}_4\text{Cl(s)}$ was measured by a balance, analysed by XRD, dissolved in deionized water and detected with the UV-vis method. The collection efficiency of $\text{NH}_4\text{Cl(s)}$ from the acid trap was calculated by equation as follow:

$$\text{Collected } NH_4Cl(s) \text{ from acid trap} = \frac{\text{collected dried out } NH_4Cl(s) \text{ (mol)}}{\text{acid collected } NH_3 \text{ (mol)}}$$

To produce pure $NH_3(aq)$ product, 350 ml of electrolyte product from the stability test was sealed in a flask and heated to 80 °C with 2 sccm Ar purging in for 24 h. The outlet tube was submerged in an ice bath to condense the NH_3 vapour into $NH_3(aq)$. The outlet tube was connected to a sealed vial to collect $NH_3(aq)$ product and then connected to an extra 200 ml of 0.3 M HCl to trap all of the emitted $NH_3(g)$. The produced $NH_3(aq)$ product was analysed using 1H NMR (500 MHz), and quantified by the spectrophotometric method mentioned above. The condensation efficiency of the $NH_3(aq)$ product was calculated by equation as follow:

$$\text{Collected } NH_3(aq) = \frac{\text{collected } NH_3(aq) \text{ (mol)}}{(\text{collected } NH_3(aq) + \text{emitted } NH_3) \text{ (mol)}}$$

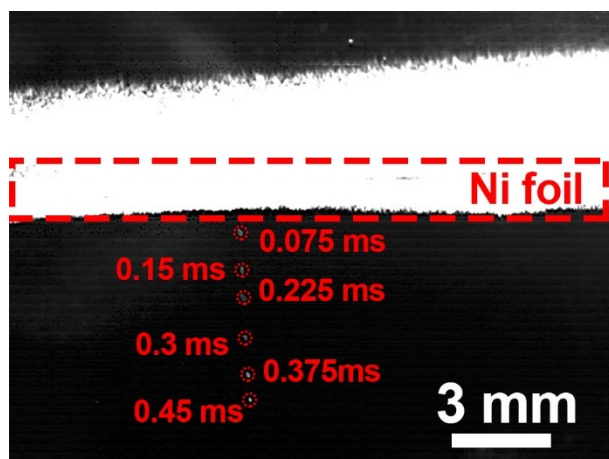
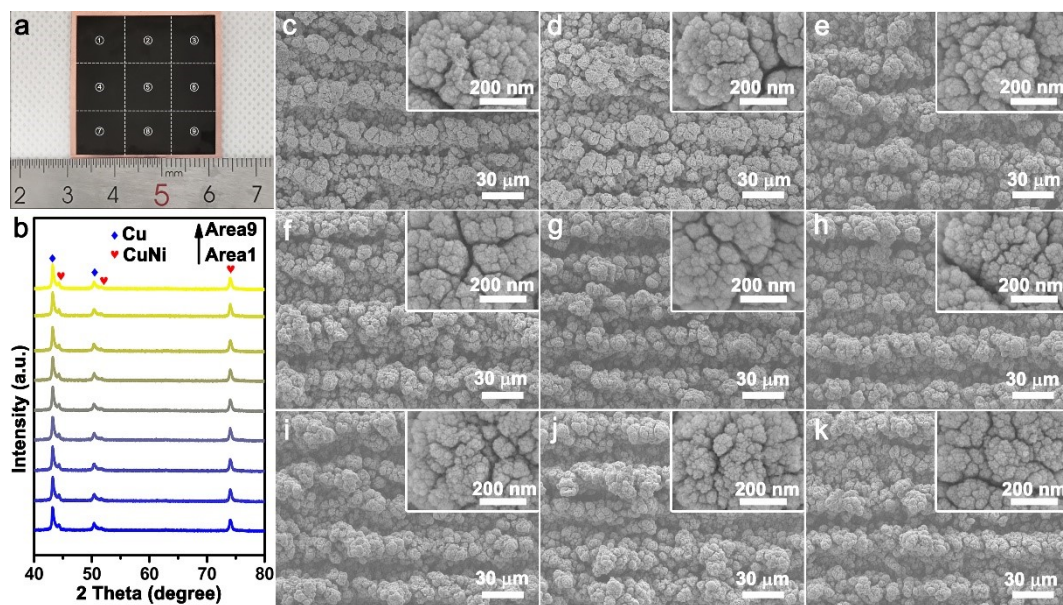
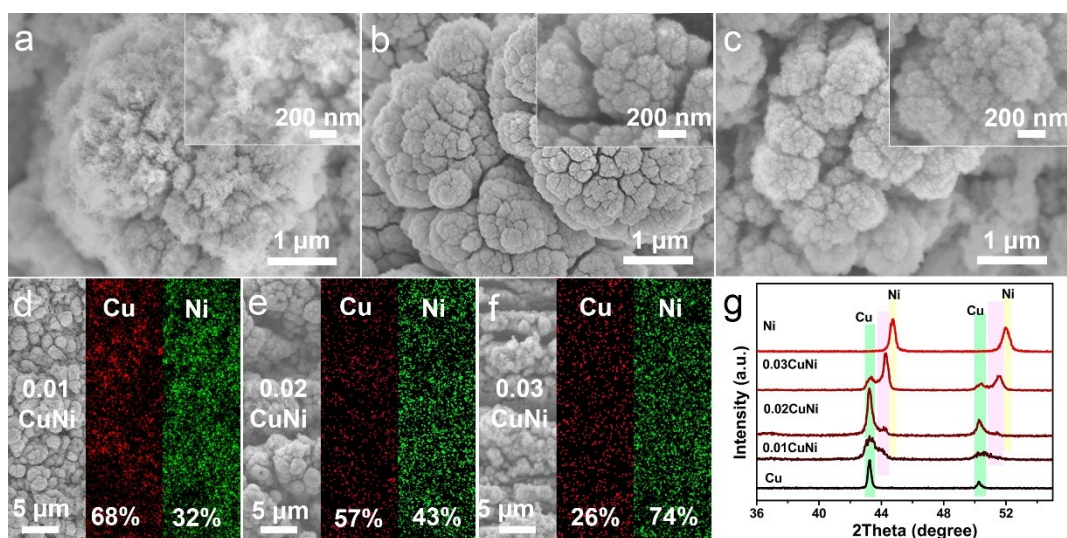


Fig. S1 High-speed camera result of laser synthesis of CuNi NPs/CF. The ms is the time unit



Uniformity of the catalyst prepared by laser irradiation

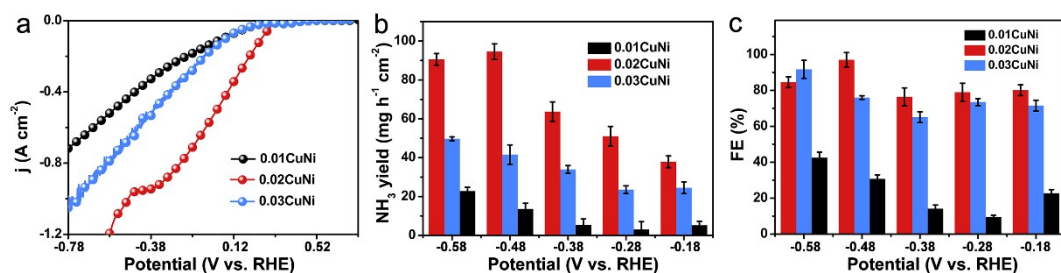
Fig. S2 (a) Digital image of CuNi NPs/CF with the area of 3*3 cm². (b) XRD corresponding to areas 1 to 9 in (a). (c-k) SEM images corresponding to areas 1 to 9 in (a).



Effects of the thickness of Ni foil on the morphology and crystal structure

Fig. S3 (a-c) SEM images, (d-e) SEM images and corresponding EDS elemental mappings and (g) XRD results of catalysts prepared with different thickness of Ni foil (0.01 mm, 0.02 mm and 0.03 mm).

XRD results showed that the diffraction peak attributed to CuNi alloy was very weak when the thickness of Ni foil was 0.01 mm. When increasing the thickness of Ni foil from 0.01 to 0.03 mm, the intensity of the diffraction peak of CuNi alloy gradually increased and the position of the peak gradually shifted from pure Cu to pure Ni. In addition, obvious diffraction peaks of Cu were observed in all samples because of the substrate of Cu.



Effects of the thickness of Ni foil on NIRR performance of catalysts

Fig. S4 (a) LSV curves, (b) NH₃ yield rates and (c) FEs of catalysts prepared with different thickness of Ni foil above.

The effects of the thickness of Ni foil on NIRR performance of catalysts were verified by electrochemical test in 1.0 M NaOH with 44.3 g L⁻¹ NO₃⁻.

The electrochemical performance results showed that the nitrate reduction performance of the catalysts reached the highest at -0.48 V vs. RHE when the thickness of Ni foil was 0.02 mm, so the subsequent experiments were carried out under this thickness.

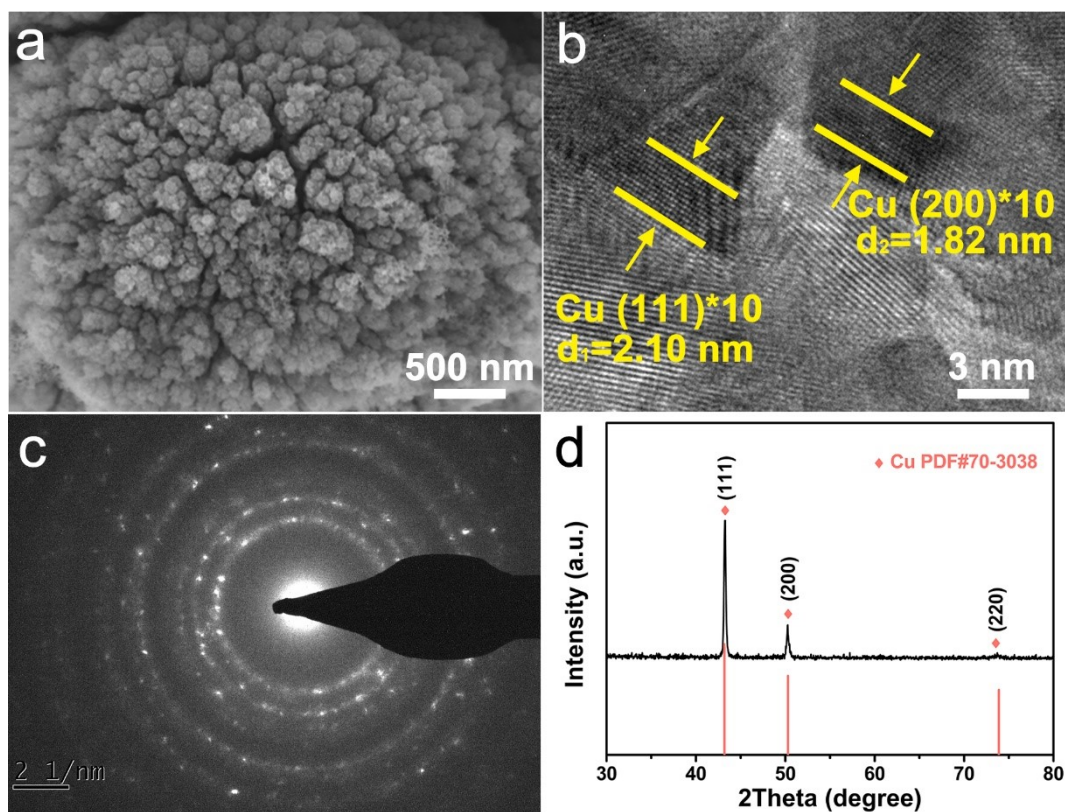


Fig. S5 (a) FESEM image, (b) TEM image, (c) SAED pattern and (d) XRD of Cu NPs/CF.

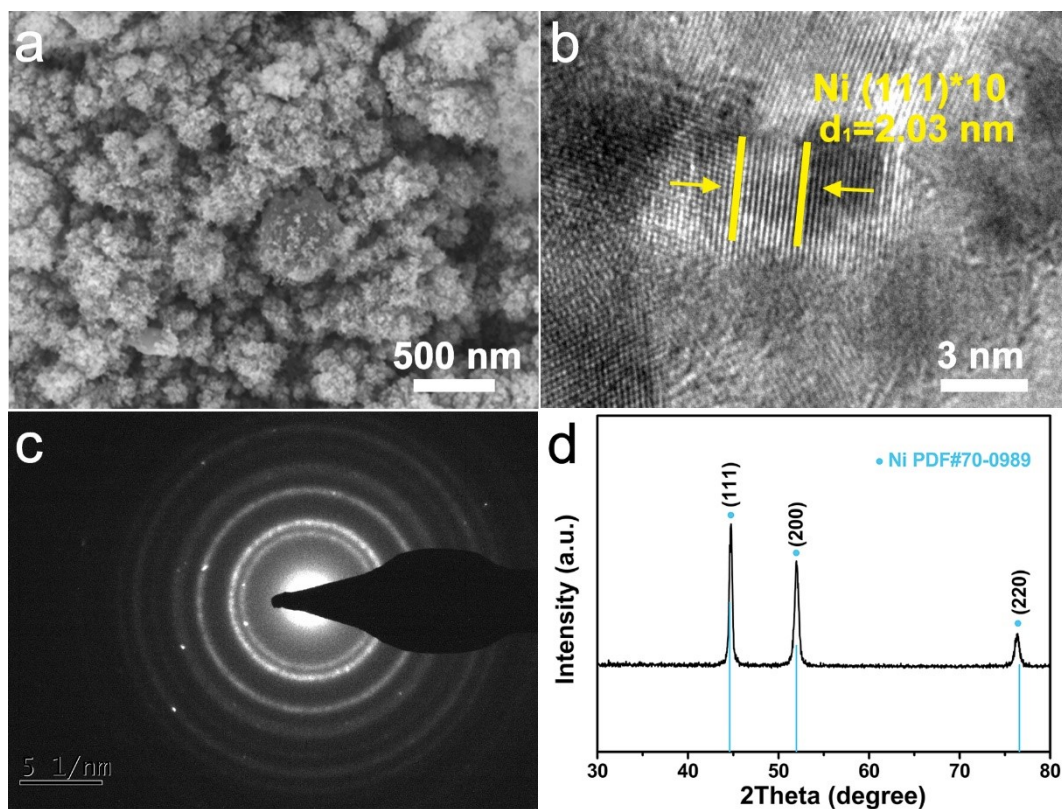


Fig. S6 (a) FESEM image, (b) TEM image, (c) SAED pattern and (d) XRD of Ni NPs/NF.

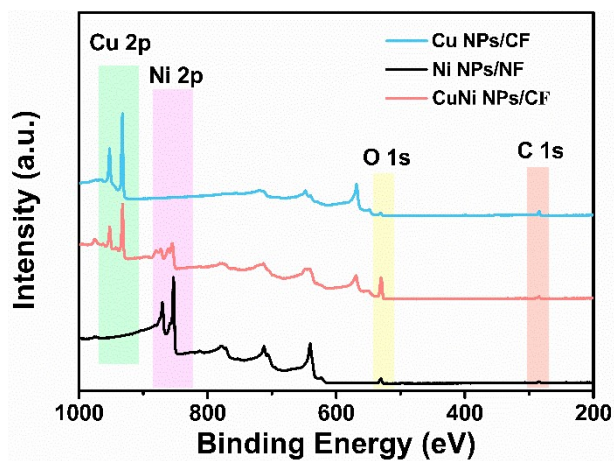


Fig. S7 XPS survey spectra of Cu NPs/CF, Ni NPs/NF and CuNi NPs/CF

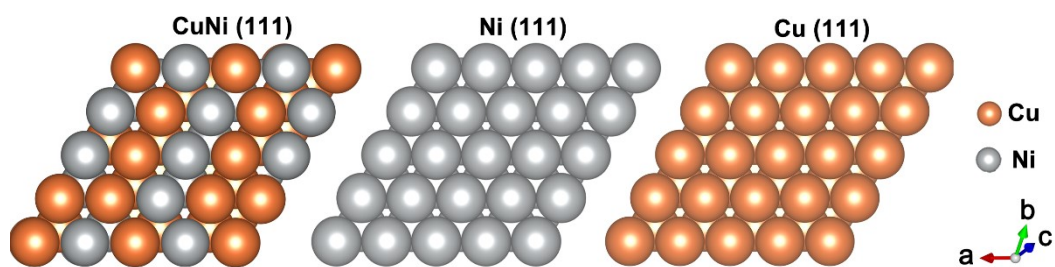


Fig. S8 Optimized structures of CuNi (111), Ni (111) and Cu (111) for DFT calculations.

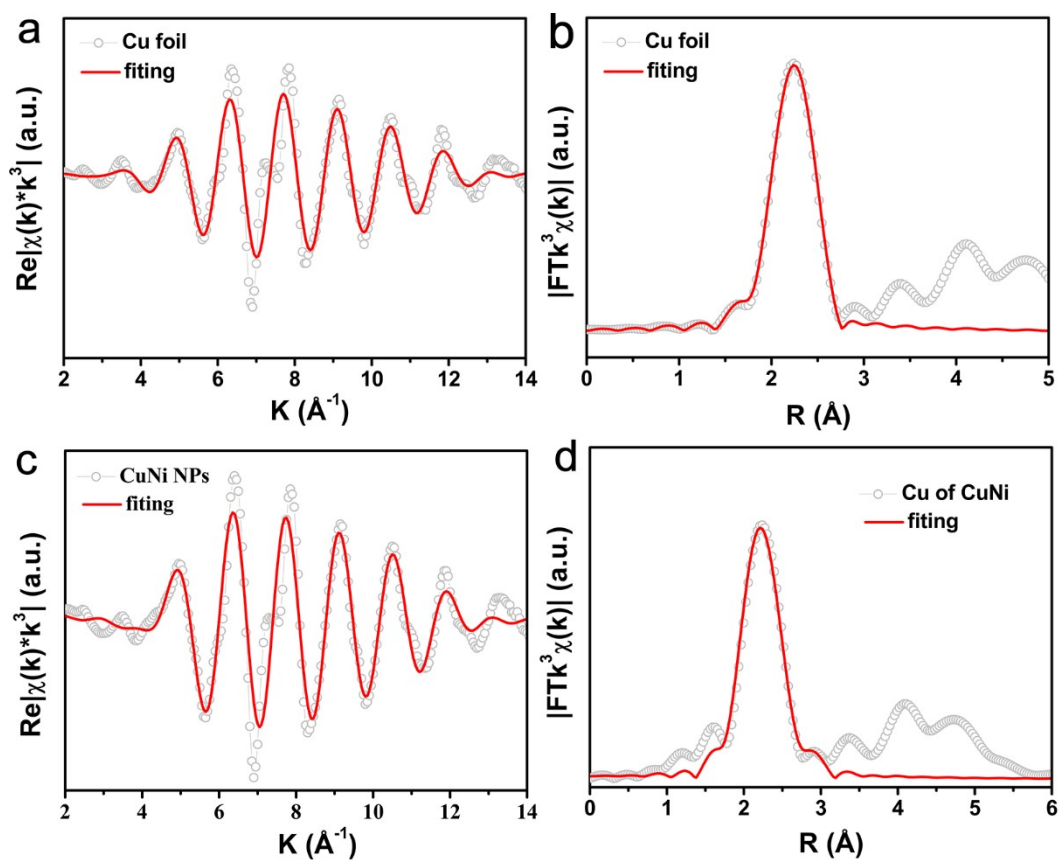


Fig. S9 (a) The fitted curve of $k^3\chi(k)$ oscillation functions in k -space and (b) its Fourier transforms in R space for Cu foil. (c) The fitted curve of $k^3\chi(k)$ oscillation functions in k -space and (d) its Fourier transforms in R space for CuNi NPs.

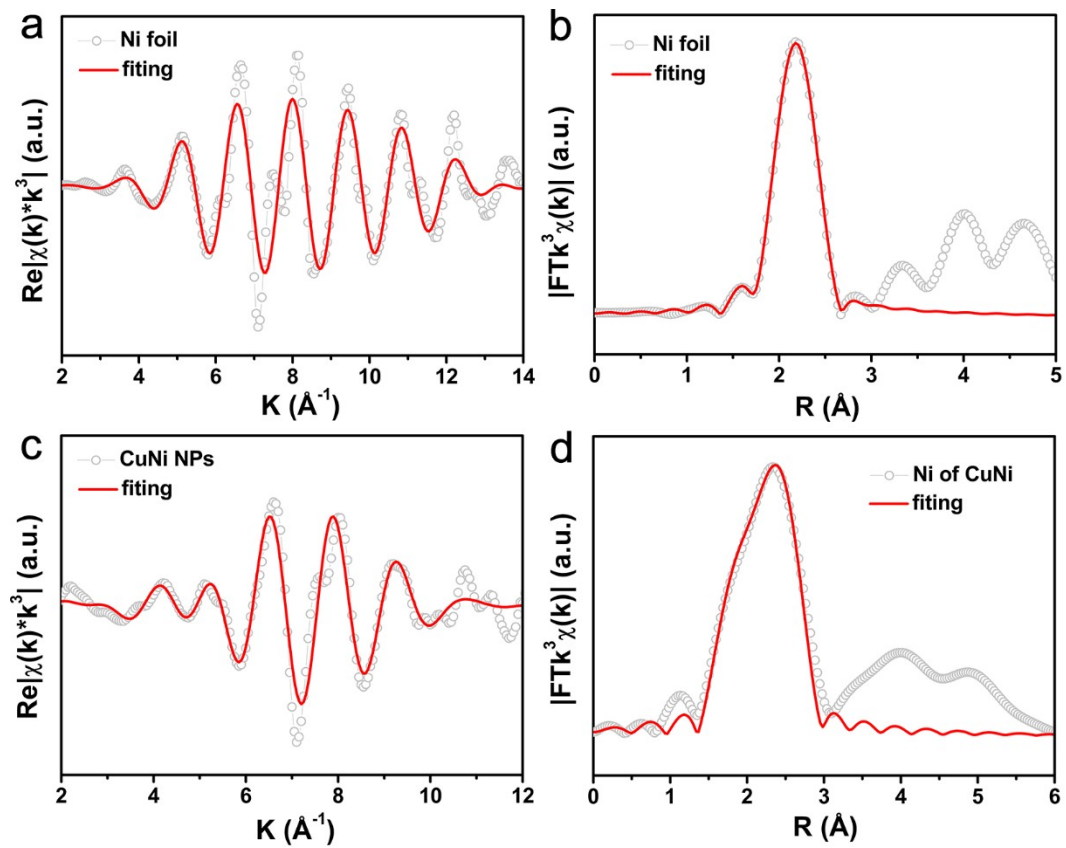
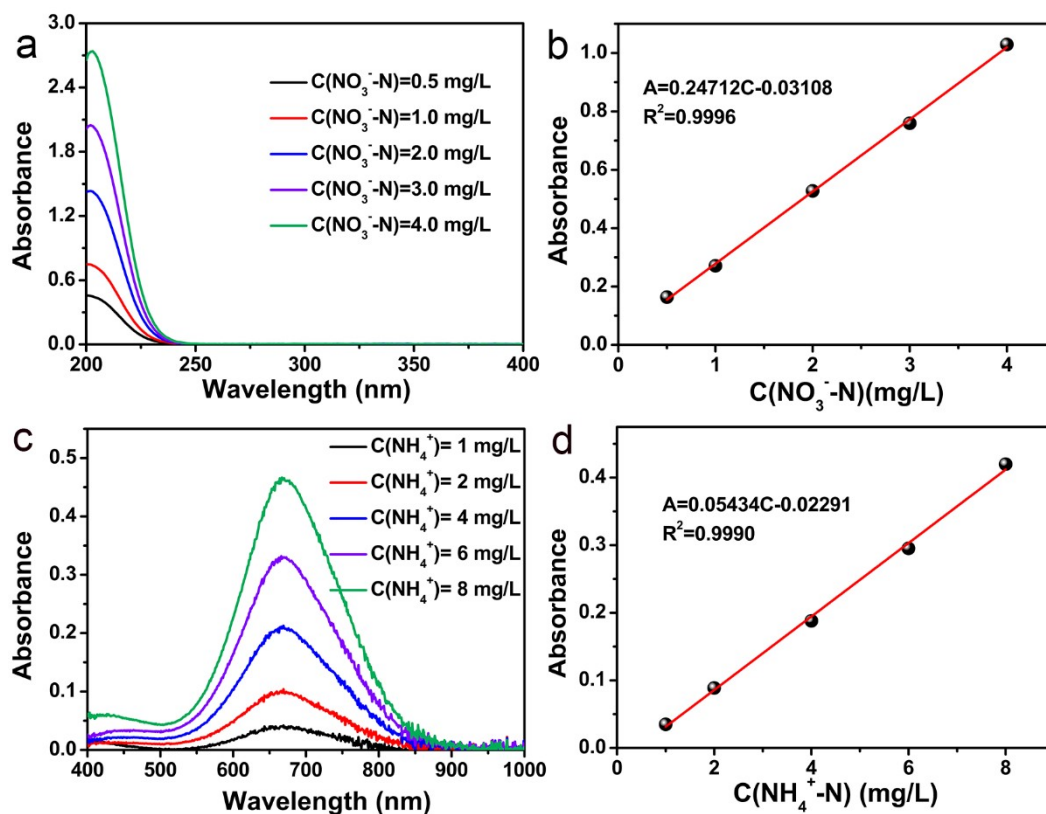


Fig. S10 (a) The fitted curve of $k^3\chi(k)$ oscillation functions in k -space and (b) its Fourier transforms in R space for Ni foil. (c) The fitted curve of $k^3\chi(k)$ oscillation functions in k -space and (d) its Fourier transforms in R space for CuNi NPs.



64

Fig. S11 The UV-visible absorption spectra of the standard solutions containing (a) NO_3^- and (c) NH_4^+ , respectively. Plotting of standard curves of (b) NO_3^- and (d) NH_4^+ . The calibration curves all show good linearity.

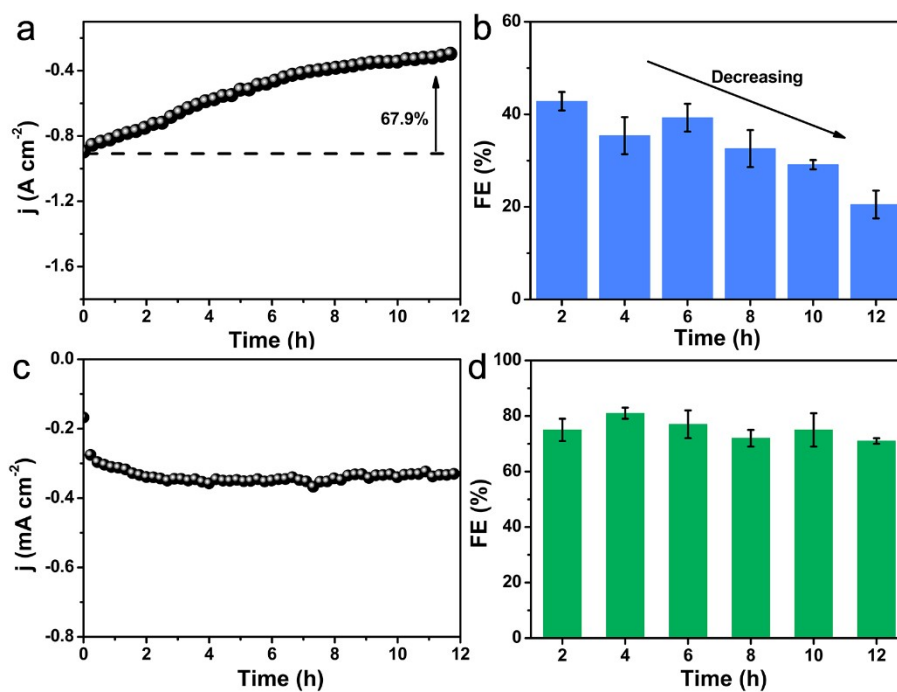


Fig. S12 (a) $i-t$ curves and (b) NH_3 FE of Cu NPs/CF at -0.48 V vs. RHE. (c) $i-t$

curves and (d) NH_3 FE of Ni NPs/NF at -0.48 V vs. RHE.

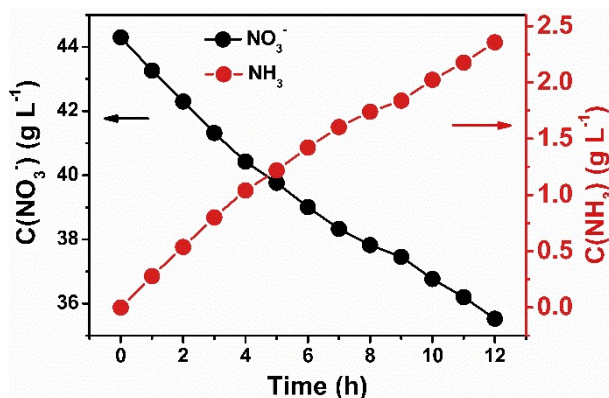


Fig. S13 Time-dependent concentration change of NO_3^- and NH_3 yield.

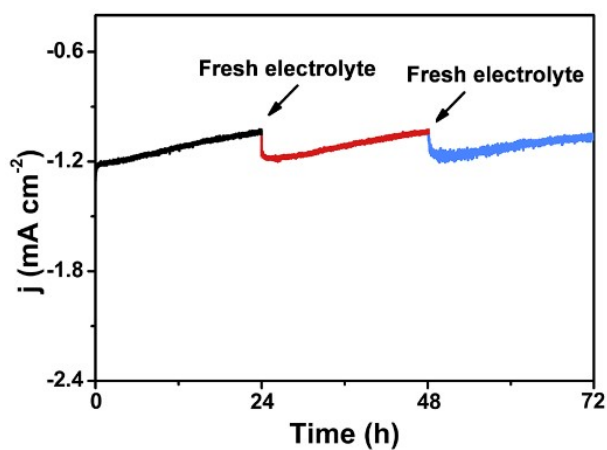


Fig. S14 I-t curves of CuNi NPs/CF at -0.48 V vs RHE in 72 h.

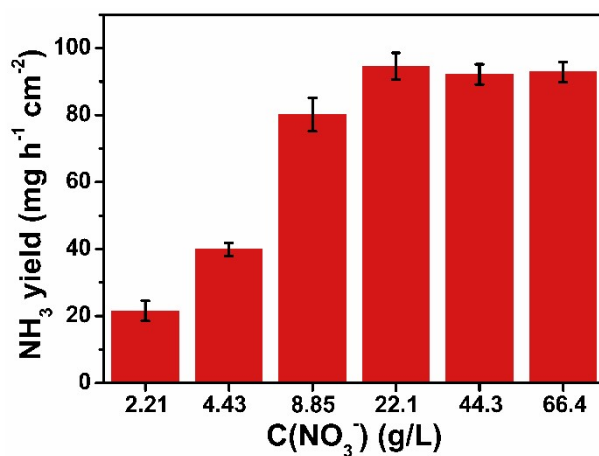


Fig. S15 The yield rate of NH_3 for CuNi NPs/CF with different concentrations of NO_3^- .

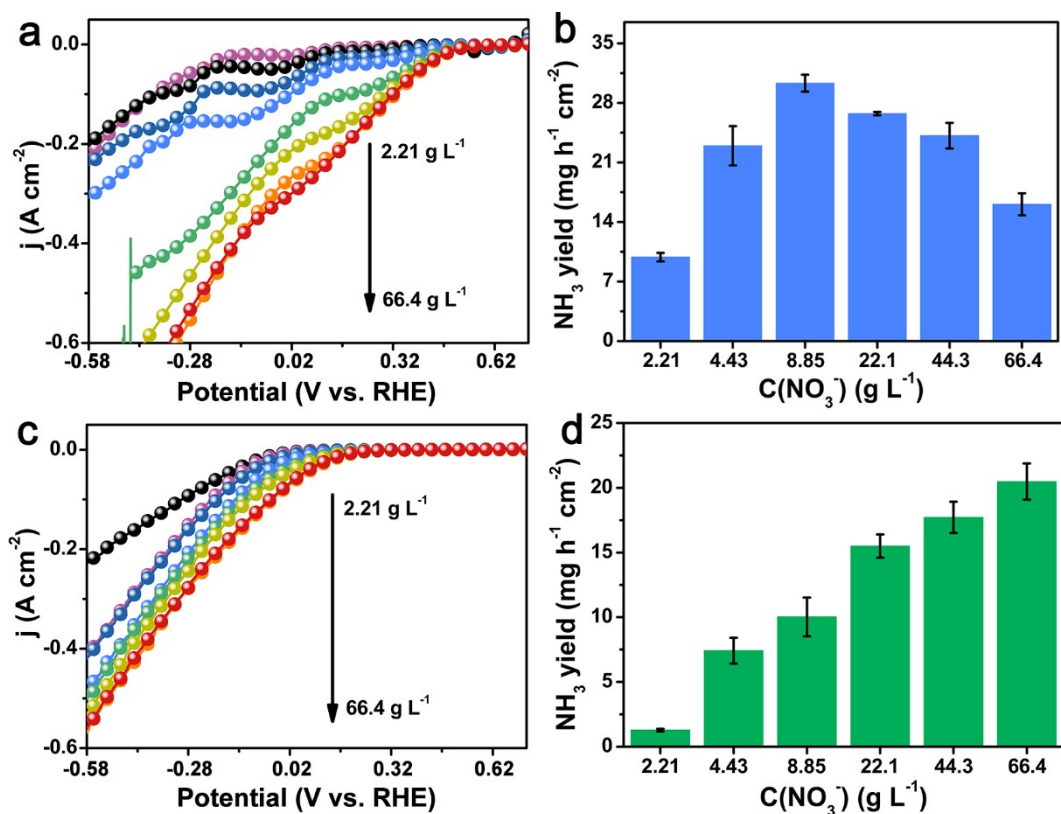


Fig. S16 The LSV curves of (a) Cu NPs/CF and (c) Ni NPs/NF with different concentrations of NO_3^- . The yield rates of NH_3 for (b) Cu NPs/CF and (d) Ni NPs/NF with different concentrations of NO_3^- .

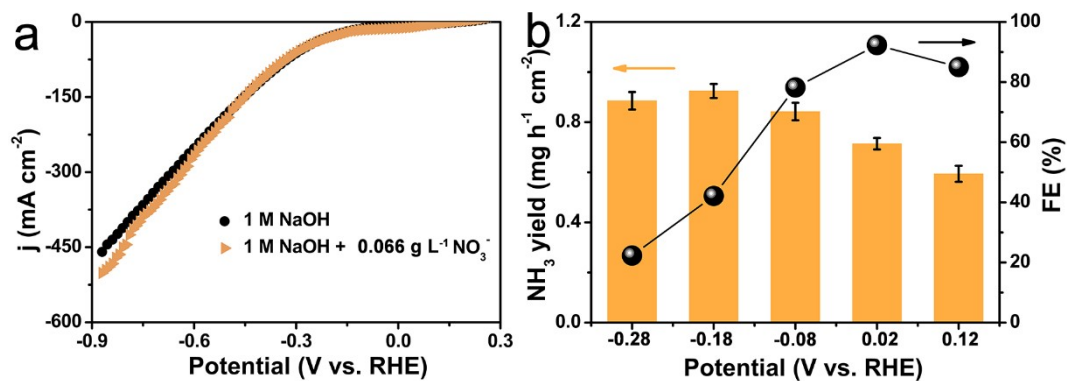


Fig. S17 (a) The LSV of CuNi NPs/CF in 1 M NaOH and 0.066 g L⁻¹ NO_3^- . (b) The yield rate of NH_3 and NH_3 FE of CuNi NPs/CF in 1 M NaOH and 0.066 g L⁻¹ NO_3^- against various potential.

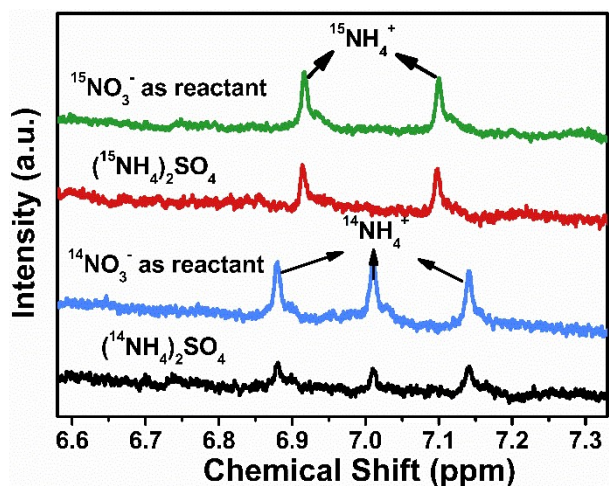


Fig. S18 ^1H NMR spectra of the electrolyte after the NIRR using $^{15}\text{NO}_3^-$ as the feedstock.

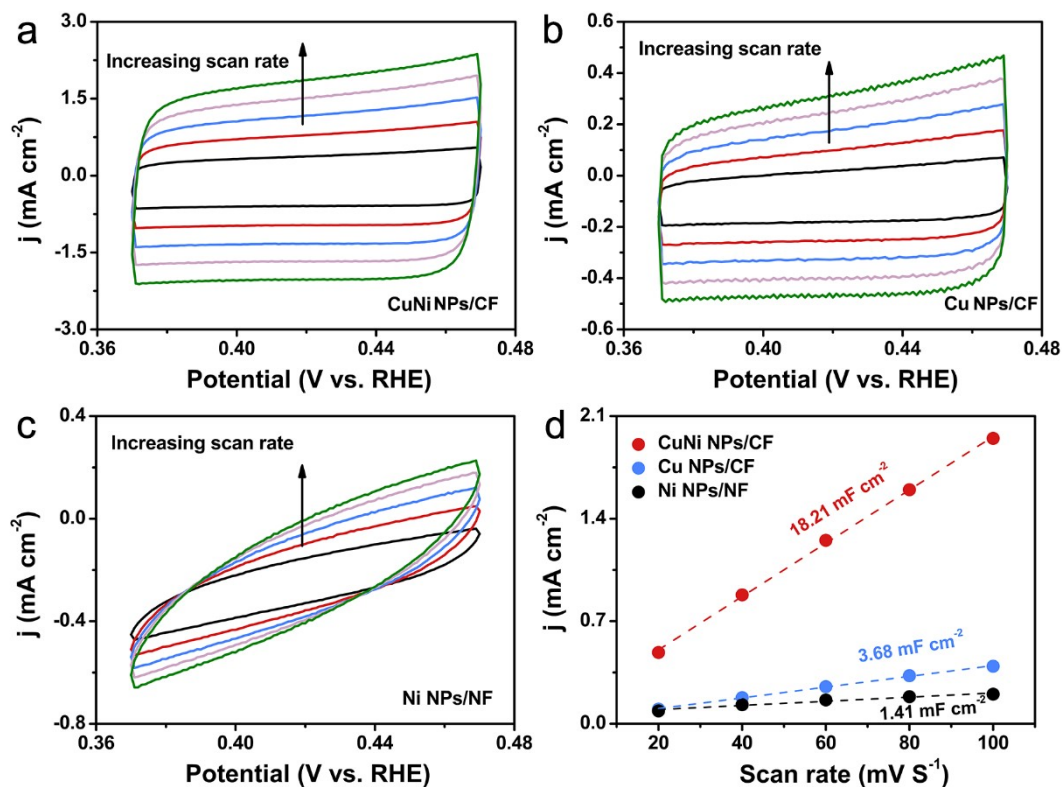


Fig. S19 CV curves of (a) CuNi NPs/CF, (b) Cu NPs/CF and (c) Ni NPs/NF in 1 M NaOH. (d) Plots of the current density versus the scan rate for the samples above.

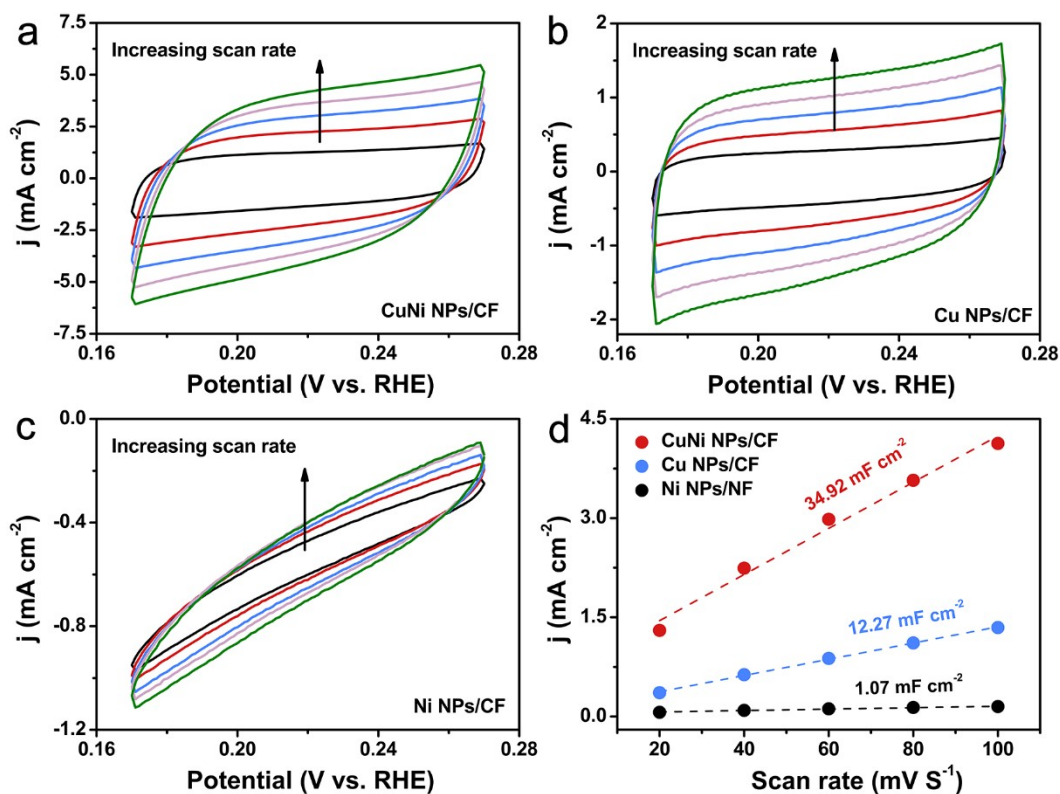
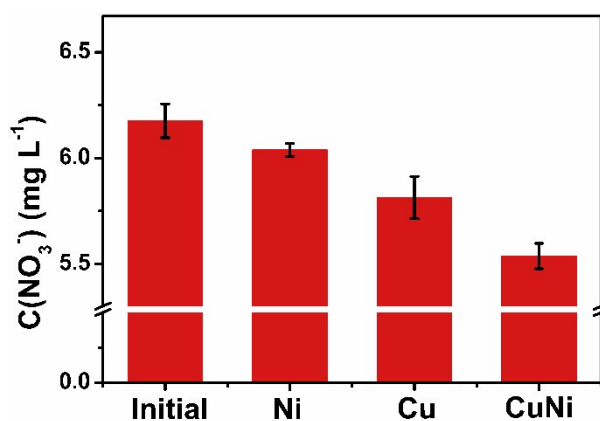


Fig. S20 CV curves of (a) CuNi NPs/CF, (b) Cu NPs/CF and (c) Ni NPs/NF in 1 M NaOH with $44.3 \text{ g L}^{-1} \text{ NO}_3^-$. (d) Plots of the current density versus the scan rate for the samples above.



Adsorption capacity test

Fig. S21 The concentration of nitrate in the electrolyte after the adsorption by Cu NPs/CF, Ni NPs/NF and CuNi NPs/CF

In order to test the adsorption capacity of the catalysts (Cu NPs/CF, Ni NPs/NF and CuNi NPs/CF) for nitrate, the catalyst with an area of $1 \times 1 \text{ cm}^2$ was immersed in 5 mL, 6.2 mg L^{-1} nitrate solution. After conducting 200 cycles of CV testing in the no-

Faradaic range, the nitrate content in the electrolyte was detected. As shown in **Fig. S21**, after the adsorption of Ni NPs/NF, Cu NPs/CF and CuNi NPs/CF, the concentration of the nitrate solution with an initial concentration of 6.21 mg L^{-1} decreases to 6.04 mg L^{-1} , 5.81 mg L^{-1} , and 5.54 mg L^{-1} .

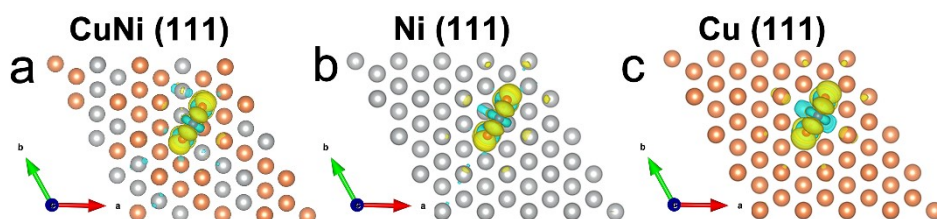


Fig. S22 The differential charge after the adsorption of $^*\text{NO}_3$ by the optimized (a) CuNi (111), (b) Ni (111) and (c) Cu (111).

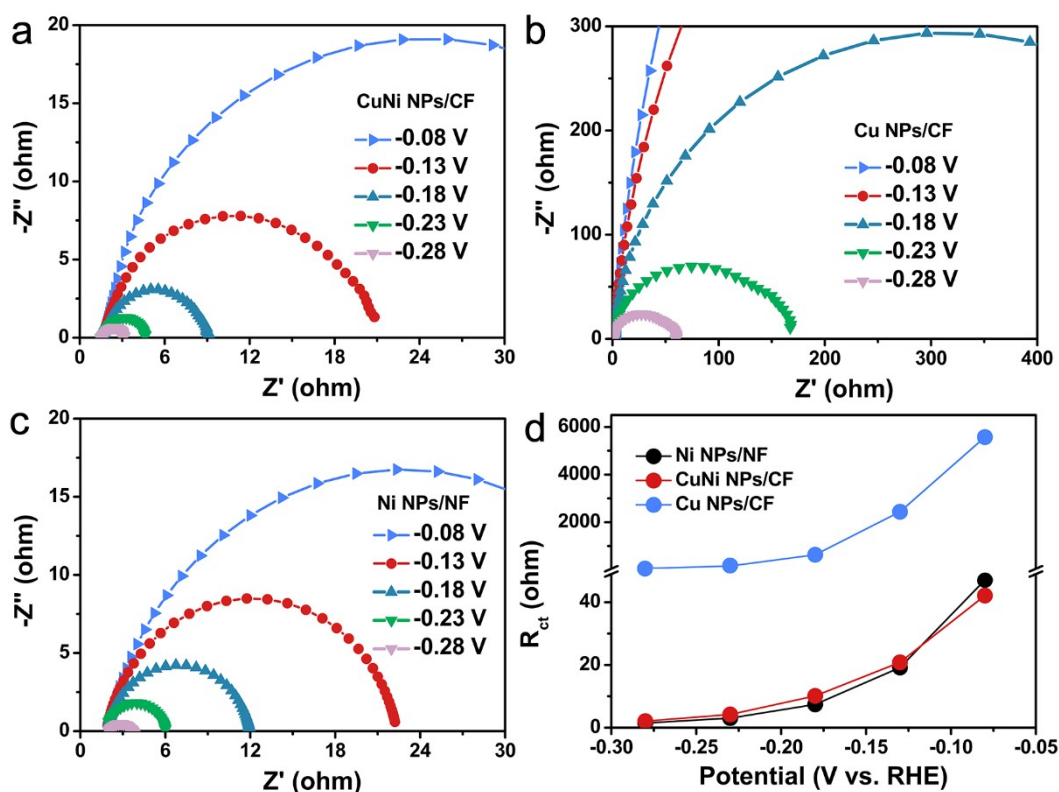


Fig. S23 The electrochemical impedance spectroscopy (EIS) Nyquist plots of (a) CuNi NPs/CF, (b) Cu NPs/CF and (c) Ni NPs/NF in 1 M NaOH. (d) The comparison of R_{ct} for the samples above in 1 M NaOH.

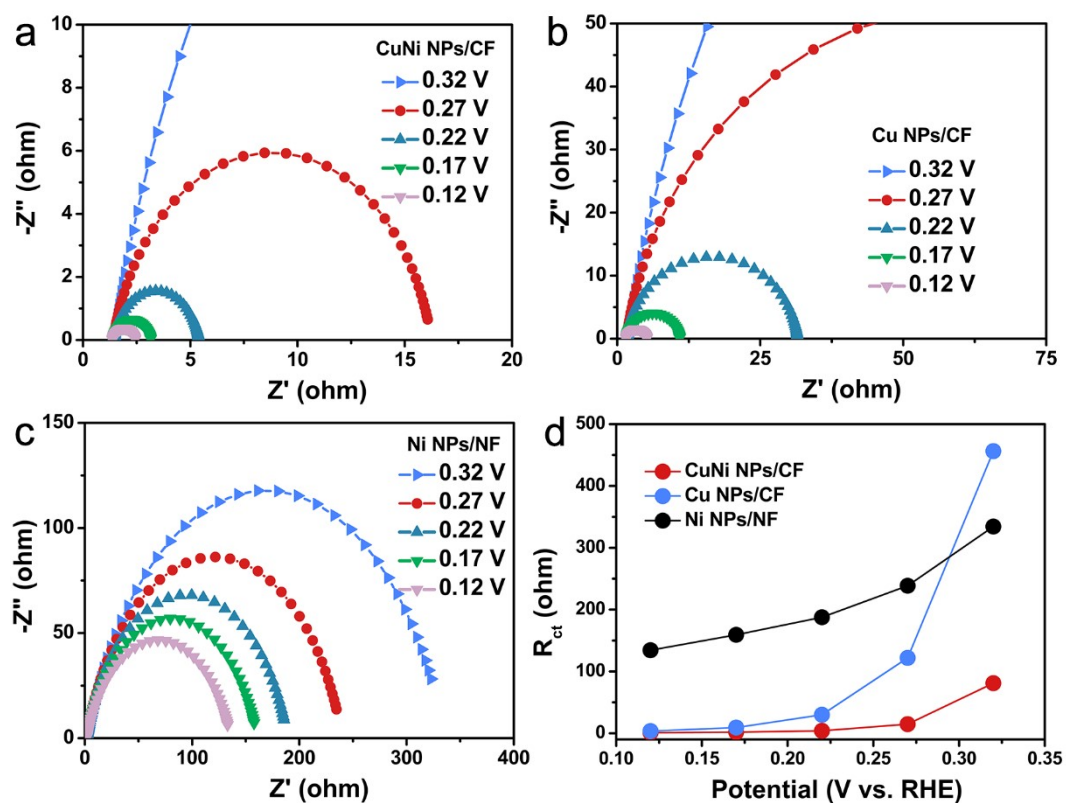


Fig. S24 The electrochemical impedance spectroscopy (EIS) Nyquist plots of of (a) CuNi NPs/CF, (b) Cu NPs/CF and (c) Ni NPs/NF in 1 M NaOH with $44.3 \text{ g L}^{-1} \text{ NO}_3^-$. (d) The comparison of R_{ct} for the samples above in 1 M NaOH with $44.3 \text{ g L}^{-1} \text{ NO}_3^-$.

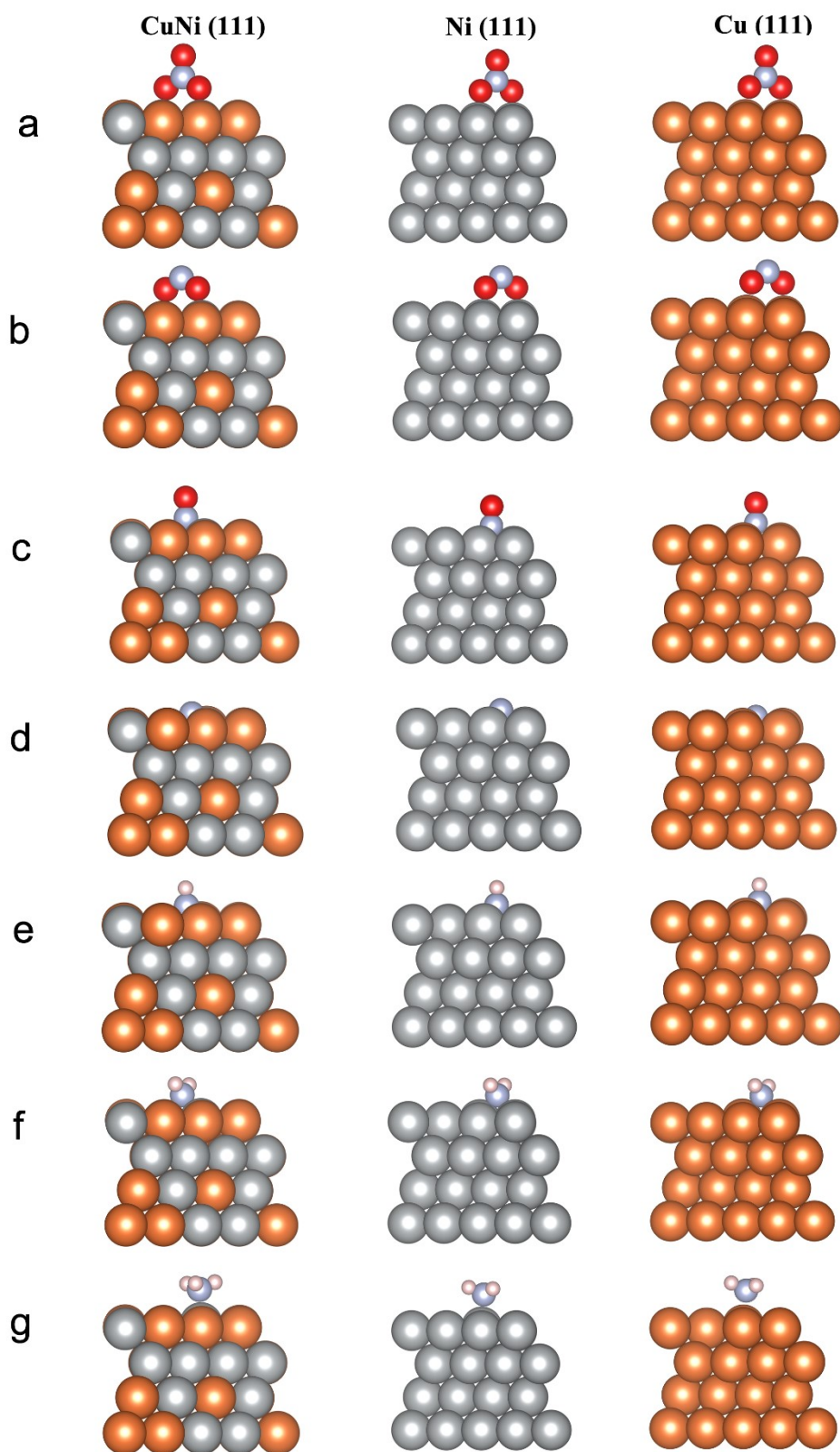


Fig. S25 Calculation models of adsorbed intermediates.

Most stable geometry with adsorbed (a) *NO_3 , (b) *NO_2 , (c) *NO , (d) *N , (e) *NH (f) *NH_2 and (g) *NH_3 on CuNi (111), Ni (111) and Cu (111), respectively.

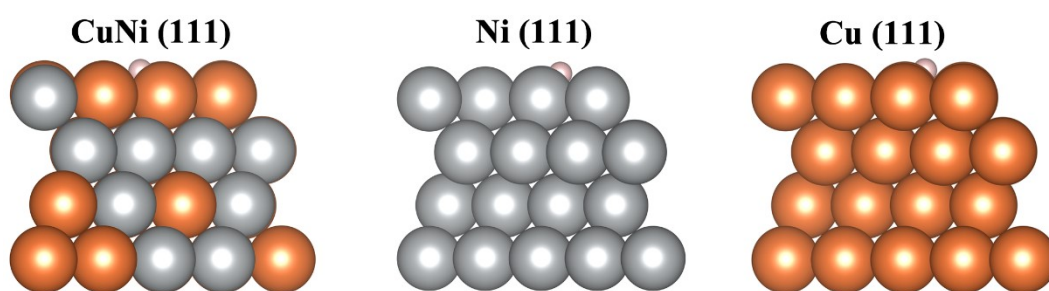


Fig. S26 Calculation model of adsorbed intermediate.

Most stable geometry with adsorbed H^* on CuNi (111), Ni (111) and Cu (111).

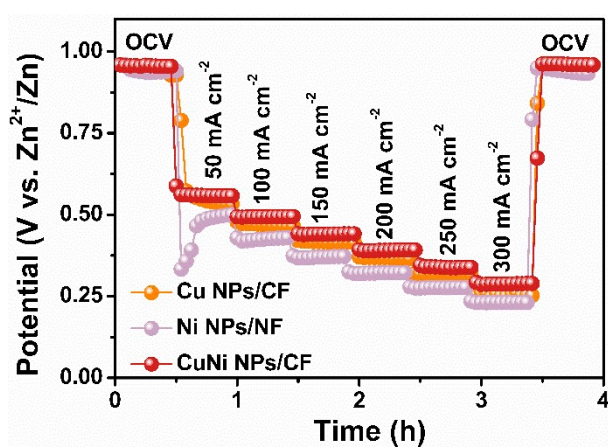


Fig. S27 The discharging tests at various current densities of the $Zn-NO_3^-$ battery with Cu NPs/CF, Ni NPs/NF and CuNi NPs/CF as the cathode in 3.5 M NaOH with $44.3 \text{ g L}^{-1} NO_3^-$.

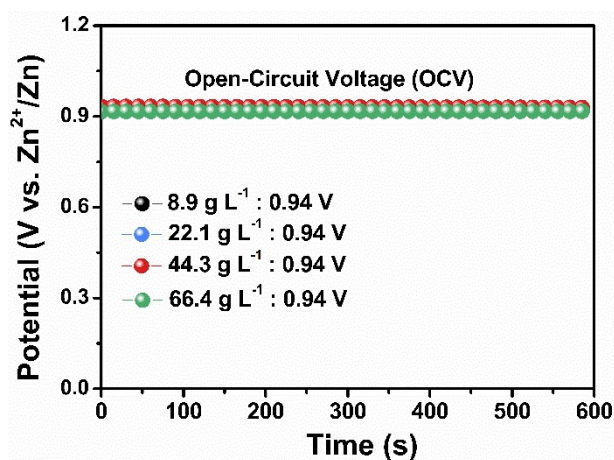


Fig. S28 The open circuit voltages of CuNi NPs/CF in 3.5 M NaOH with different concentrations of NO_3^- .

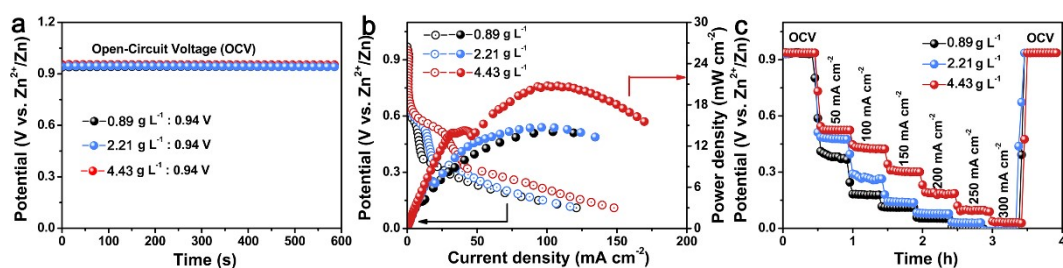


Fig. S29 (a) The open circuit voltages, (b) the discharging polarization curves and the resultant power densities, and (c) discharging tests of CuNi NPs/CF at various current densities of the Zn-NO₃⁻ battery in 3.5 M NaOH with 0.89-4.43 g L⁻¹ NO₃⁻.

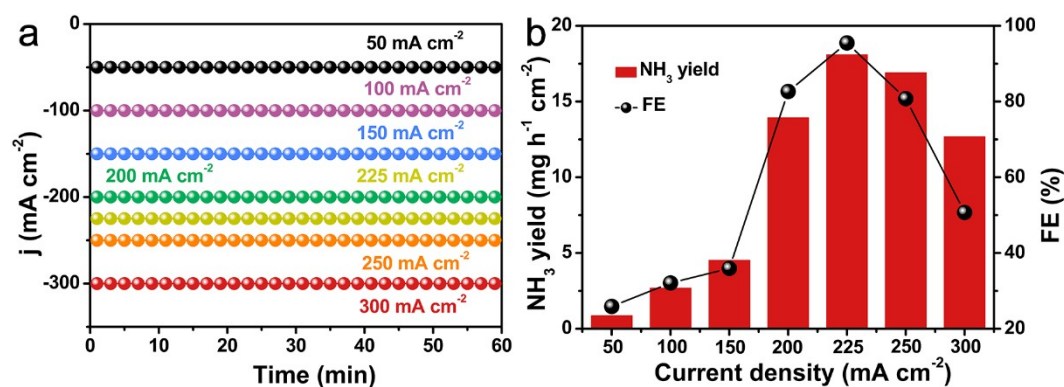


Fig. S30 NIRR performance of the Zn-NO₃⁻ battery assembled by CuNi NPs/CF as the cathode at various current densities of in 3.5 M NaOH with 44.3 g L⁻¹ NO₃⁻. (a) i-t curves at different current densities. (b) The NH₃ yield and the corresponding FE derived from the Zn-NO₃⁻ battery system

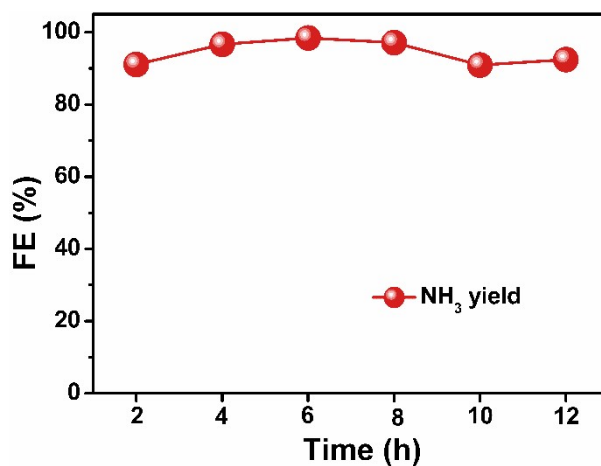


Fig. S31 NH_3 FE of Zn-NO_3^- battery system using CuNi NPs/CF against various work time after the long-term NIRR experiment.

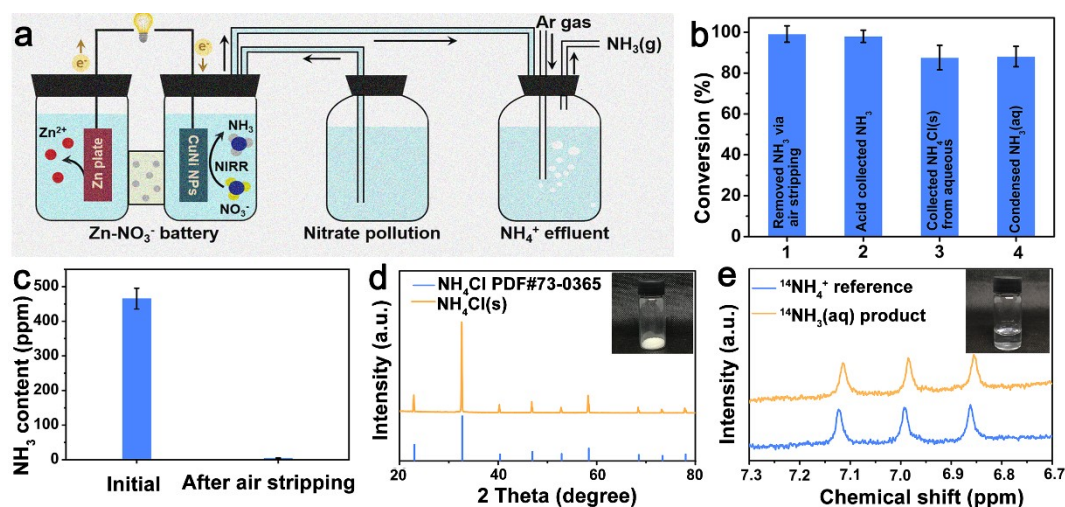



Fig. S32 Practical NH_3 products synthesis. (a) Schematic of the NH_3 product synthesis process from NO_3^- -containing influent. (b) Conversion efficiency of different steps for the ammonia product synthesis process. (c) NH_3 content in electrolyte collected before and after stripping. (d) Synthesized $\text{NH}_4\text{Cl}(\text{s})$ products and its XRD analysis result. (e) ^1H NMR analysis of the synthesized $\text{NH}_3(\text{aq})$. Inset: the products itself.


With the impressive NIRR performance of Zn-NO_3^- battery by CuNi NPs/CF as the cathode, we further demonstrated its practical applications by coupling the Zn-NO_3^- battery with an air stripping method to continuously collect high-purity NH_3 products (**Fig. S32a**). Taking advantage of the high vapour pressure of NH_3 in the alkaline electrolyte, the method of stripping was employed to realize the efficient separation of NH_3 produced by NO_3^- reduction in the effluent. The collection efficiency of acid solution for NH_3 was more than 98% (**Fig. S32b**), and high-purity ammonium chloride ($\text{NH}_4\text{Cl}(\text{s})$) powder was prepared by combining with the rotary evaporation process. After separation, more than 99.1% of the NH_3 in the effluent was extracted, and the residual NH_3 in the effluent was only 4.39 ppm, which indicated that our Zn-NO_3^- battery effectively converted NO_3^- in the sewage while outputting electric energy, and synthesized NH_3 with high added value at the same time (**Fig. S32c**). The separated NH_3 was collected by the capture of a HCl solution or condensation. As

shown in **Fig. S32d**, the XRD confirmed the synthesis of pure $\text{NH}_4\text{Cl(s)}$, which was widely used in agricultural production as an important fertilizer. In addition, the solution with $\text{NH}_3(\text{aq})$ concentration up to 0.53 wt% was obtained by condensing the steam containing NH_3 . The generation of $\text{NH}_3(\text{aq})$ was identified by ^1H NMR spectroscopy (**Fig. S32e**). The yield rate of each product was analyzed by UV-Vis spectrum and the collection efficiency of each step was calculated (**Fig. S33, S34**). The overall collection efficiency of both products is over 85% (**Fig. S32b**). Overall, we demonstrated a complete process that directly converts NO_3^- -containing influent into practical NH_3 products using our Zn-NO_3^- battery by CuNi NPs/CF as the cathode, accompanied by the output of electric energy.



Initial $\text{NH}_4\text{Cl(s)}$ in outlet product (mg)	Collected $\text{NH}_4\text{Cl(s)}$ solid (mg)	$\text{NH}_3(\text{s})$ collection efficiency
464.4	396.3	85.4%
502.1	449.9	89.6%
485.8	427.0	87.9%
		Average: 87.6%

Fig. S33 Collected $\text{NH}_4\text{Cl(s)}$ (left hand side) and their mass and collection efficiency (right hand side) from 3 individual tests.



Collected $\text{NH}_3(\text{aq})$ (mg)	Emitted NH_3 (mg)	$\text{NH}_3(\text{aq})$ collection efficiency
14.6	1.2	92.4%
16.1	3.3	83.3%
15.5	2.0	88.5%
		Average: 88.1%

Fig. S34 Collected $\text{NH}_3(\text{aq})$ (left hand side) and their mass and collection efficiency (right hand side) from 3 individual tests

Table S1. The proportion of Cu and Ni in the CuNi NPs/CF characterized by ICP-MS

Elements	Instrument readings	Units	Converted contents	Units	Mass fractions (wt%)
Cu	10.230	mg/L	606019.0	mg/kg	60.6019
Ni	6.5783	mg/L	389706.8	mg/kg	38.9706

Table S2 The comparison of the NH₃ yields and FEs of CuNi NPs/CF with the reported catalysts for NIRr.

Catalyst	NH ₃ FE (%)	NH ₃ Yield (mg cm ⁻² h ⁻¹)	Electrolyte	Reduction Potential	Reference
CuNi NPs/CF	97.03	94.57	1 M NaOH + 44.3 g L ⁻¹ NO ₃ ⁻	-0.48 V (vs. RHE)	This Work
Co 3D NA	86.2	68.4	1 M KOH + 2000 ppm KNO ₃	/	<i>Nature Commun.</i> , 2023, 14:1619.
Cu-RD-KOH	100	3.06	0.1 M KOH + 500 ppm NO ₃ ⁻	-0.2 V (vs. RHE)	<i>Angew. Chem. Int. Ed.</i> 2023, e202218717
CuRu	98	6.46	1M KOH + 0.1 M KNO ₃	-0.05 V (vs. RHE)	<i>Adv. Mater.</i> , 2023, 2202952.
CuCo	100	81.6	1 M KOH + 0.1 M KNO ₃	-0.2 V (vs. RHE)	<i>Nat. Commun.</i> , 2022, 13, 7899
ox-LIG	100	48.6	1 M NaNO ₃	-0.93 V (vs. RHE)	<i>Adv. Mater.</i> , 2023, 2211856
Ru-CuNW	96	76.5	1 M KOH + 2000 ppm NO ₃ ⁻	-0.135 V (vs. RHE)	<i>Nature Nanotech.</i> , 2022, 17, 759–767
NiO ₄ -CCP	94.7	12.8	1 M KOH + 0.1 M KNO ₃	-0.7 V (vs. RHE)	<i>Adv. Mater.</i> 2023, 2209855
CoRu	99	23.6	1 M KOH + 0.1 M KNO ₃	/	<i>Angew. Chem. Int. Ed.</i> 2023, e202300390
FeB ₂	96.8	25.5	1 M KOH + 0.1 M KNO ₃	-0.6 V (vs. RHE)	<i>Angew. Chem. Int. Ed.</i> 2023, e202300054
Ni ₃ Fe-CO ₃ LDH/Cu foam	96.8	1.26	1 M KOH + 5 mM KNO ₃	-0.2 V (vs. RHE)	<i>Energy Environ. Sci.</i> , 2023,16,

Table S3. Comparison of CuNi NPs/CF in this work with other reported CuNi alloys

Catalyst	NH ₃ FE (%)	NH ₃ Yield (mg cm ⁻² h ⁻¹)	Electrolyte	Reduction Potential	Reference
CuNi NPs/CF	97.03	94.57 (Ampere-level)	1 M NaOH + 44.3 g L ⁻¹ NO ₃ ⁻	-0.48 V (vs. RHE)	This Work
Cu _{0.25} Ni _{0.25}	94.5	9.34	1 M KOH + 75 mM KNO ₃	-0.3 V (vs. RHE)	<i>Dalton Trans.</i> , 2022, 51, 15111
CuNi/NC	79.6	Around 15 mA cm ⁻²	0.1 M PBS+ 50 ppm NO ₃ ⁻ -N	-1.1 V (vs. Ag/AgCl)	<i>J. Colloid Interface Sci.</i> , 614 (2022) 405–414
CuNi/OMC	78.9	2.37	0.1 M PBS + 500 ppm KNO ₃	-0.4 V (vs. RHE)	<i>ACS Sustainable Chem. Eng.</i> , 2023, 11, 2468–2475
Cu ₅₀ Ni ₅₀ -Ar plasma	100	6.0	1 M KOH + 0.1 M KNO ₃	-0.27 V (vs. RHE)	<i>Waste Disposal & Sustainable Energy</i> (2022) 4: 149–155
Cu/Ni-NC	97.3	5.48	0.5 M Na ₂ SO ₄ + 100 ppm NaNO ₃	-0.7 V (vs. RHE)	<i>Small</i> 2023, 2207695
Cu ₅₀ Ni ₅₀	99	Around 100 mA cm ⁻²	1 M KOH + 0.1 M KNO ₃	-0.1 V (vs. RHE)	<i>J. Am. Chem. Soc.</i> 2020, 142, 5702–5708

Table S4. Reaction free energies of NIRR for different intermediates on different models of CuNi (111), Ni (111) and Cu (111).

	CuNi (111)	Ni (111)	Cu (111)
*	0	0	0
*NO ₃ ⁻	-0.16	0.44	0.3
*NO ₂	-1.27	-1.00	-0.67
*NO	-2.12	-2.28	-0.63
*N	-1.95	-2.27	-0.91
*NH	-2.15	-2.26	-1.93
*NH ₂	-2.07	-2.00	-1.57
*NH ₃	-1.87	-1.84	-1.43
NH ₃	-1.55	-1.55	-1.55

Table S5. Reaction free energies of HER for different intermediates on different models of CuNi (111), Ni (111) and Cu (111).

	CuNi (111)	Ni (111)	Cu (111)
*	0	0	0
*H	-0.36	-0.32	0.21
H ₂	0	0	0

Table S6. The comparison of the OCV and the maximum power density with the reported catalysts for Zn-NO_x^{y-}batteries.

Catalyst	OCV (V)	NH ₃ yield (mg h ⁻¹ cm ⁻² (mg ⁻¹))	Power density (mW cm ⁻²)	Electrolyte	Reference
CuNi NPs/CF	0.94	18.1	70.7	3.5 M NaOH 3.5 M NaOH + 44.3 g L ⁻¹ NO ₃ ⁻	This Work
Ru-25CV/NF	1.2	2.9	51.5	1.0 M KOH + 1.0 M NaNO ₃	<i>Small</i> , 2022, 18, 2200436
NiCoBDC@HsGDY	1.47	1.125	3.66	6 M KOH 1 M KOH + 0.1 M NO ₃ ⁻	<i>ACS Nano</i> , 2023, 10.1021/acsnano.2c12491
Cu-RD	0.943	15.5	14.09	1 M KOH 1 M KOH + 0.5 M NO ₃ ⁻	<i>Angew. Chem. Int. Ed.</i> , 2023, e202218717
Ru/β-Co(OH) ₂	1.48	6.46	29.87	6 KOH 1 M KOH + 0.1 M KNO ₃	<i>Energy Environ. Sci.</i> , 2023, 10.1039/D3EE00371J
NiCo ₂ O ₄	1.30	0.82	3.94	6 KOH 0.1 M NaOH + 0.1 M NaNO ₃	<i>Small</i> , 2022, 2106961
Fe/Ni ₂ P	1.22	0.38	3.25	1 M KOH 0.2 M K ₂ SO ₄ + 0.05 M KNO ₃	<i>Adv. Energy Mater.</i> , 2022, 2103872
DM-Co	0.7	2.04	25.8	1 M KOH + 0.02 M Zn(CH ₃ COO) ₂ 1 M KOH + 1 M KNO ₃	<i>Adv. Funct. Mater.</i> , 2022, 32, 2209464
Fe ₂ TiO ₅	1.5	0.56	5.6	\	<i>Angew. Chem. Int. Ed.</i> , 2022, e202215782
MP-Cu	1.27	1.29	7.56	5 M KOH 1 M KOH + 0.05 M NO ₃ ⁻	<i>Adv. Funct. Mater.</i> , 2023, 33, 2212236.